

Insight into Doping Effects in Apatite Silicate Ionic Conductors**

By Julian R. Tolchard, Peter R. Slater, and M. Saiful Islam*

Novel apatite-type silicates are attracting considerable interest as a new family of oxide-ion conductors with potential use in fuel cells and ceramic membranes. Combined computer modeling and X-ray absorption (EXAFS) techniques have been used to gain fresh insight, at the atomic level, into the site selectivity and local structures of a wide range of dopants in these apatite materials. The results indicate that an unusually broad range of dopant ions (in terms of size and charge state) can substitute for La in the $\text{La}_{9.33}\text{Si}_6\text{O}_{26}$ apatite, in accord with current experimental data. The range is much wider than that observed for doping on a single cation site in most other oxide-ion conductors, such as the perovskite LaGaO_3 . In addition, our local structural investigation demonstrates that this dopant behavior is related to the flexibility of the silicate substructure, which allows relatively large local distortion and alteration of the site volumes. This could be a key factor in the high oxide-ion conductivity exhibited by these apatite silicates. Indeed, the breadth of possible doping regimes in these novel materials provides new opportunities to design and optimize the conduction properties for fuel cell electrolytes.

1. Introduction

The development of new oxide-ion conducting materials is a pressing scientific and technological need as they form the basis of a range of important environmentally friendly applications such as sensors, gas separation membranes, and solid oxide fuel cells (SOFCs). This latter example in particular is being intensively studied, as the high efficiency of SOFCs and their ability to act as a bridging technology between hydrocarbon- and hydrogen-fuel technologies makes them prime candidates for next generation power production.^[1,2]

To date, oxide materials exhibiting the fluorite or perovskite structures, such as doped ZrO_2 and doped LaGaO_3 , have dominated research in this area.^[2,3] Recently, however, a range of rare-earth apatite materials have been proposed as alternative solid electrolyte materials following the exciting discovery of fast oxide-ion conductivity in these silicate systems.^[4–18] Iso-

structural with the well-known apatite minerals and hydroxyapatite biomaterials,^[19] these materials have the general formula $\text{M}_{10}(\text{XO}_4)_6\text{O}_{2\pm y}$, where M is a metal such as a rare-earth or an alkaline-earth metal, and X is a p-block element such as P, Si, or Ge. The crystal structure (Fig. 1) comprises isolated XO_4 tetrahedra arranged so as to form two distinct channels running parallel to the c axis. Occupying the smaller of these channels are M cations, whilst the larger channel contains oxide ions.

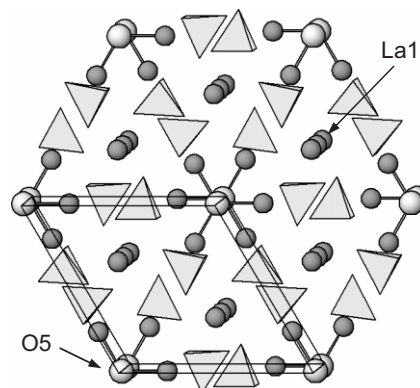


Figure 1. Structure of the apatite-type oxide $\text{La}_{10-x}\text{Si}_6\text{O}_{26}$, showing SiO_4 tetrahedra, La (gray), and O (white) ions. La(1) and O(5) channels both run parallel to the c axis.

A number of rare-earth oxyapatite systems have been synthesized, and it is the lanthanum silicate and germanate analogues that have been found to demonstrate the highest conductivities.^[4,5] The carrier species is purely anionic for most compositions, with high oxygen transference numbers ($t_{\text{O}} > 0.9$) across a wide range of oxygen partial pressures,^[4] which is sufficient for electrolyte applications. It is found that these materials are tolerant to an unusually broad range of dopants, partic-

[*] Prof. M. S. Islam
Department of Chemistry, University of Bath
Bath BA2 7AY (UK)
E-mail: m.s.islam@bath.ac.uk

Dr. P. R. Slater
Materials Chemistry Group, Chemistry Division, SBMS
University of Surrey
Guildford, GU2 7XH (UK)

Dr. J. R. Tolchard
Department of Materials Technology
Norwegian University of Science and Technology
7491 Trondheim (Norway)

[**] This work is supported by the UK Engineering and Physical Sciences Research Council (EPSRC) under grant code GR/R29239/01. The EXAFS work was performed at the SRS facilities at Daresbury Laboratory. We are grateful to Dr. E. Kendrick, Dr. C. Fisher, and Dr. L. Murphy for their assistance. Supporting Information is available online from Wiley InterScience or from the author.

ularly on the rare-earth sites, with the observed conductivity being very sensitive to the doping regime and cation/anion nonstoichiometry.^[4–13] In particular, it is found that fully stoichiometric systems, such as La₈Sr₂Si₆O₂₆, generally exhibit poor conductivity, whilst the doping of subvalent cations (such as Ga³⁺ or Al³⁺) on the Si site,^[8,10] or La substoichiometry to create vacancies in the La(1) channels,^[7] markedly improves conductivity. The highest conductivities are found for the samples containing excess oxygen, and it has thus been suggested that interstitial oxide-ion conduction occurs along the O(5) channels (Fig. 1). This hypothesis has been strengthened by neutron diffraction studies^[12] of the La_{9.33}(Si,Ge)₆O₂₆ and La₁₀Si₆O₂₇ systems, which confirm a link between fast ionic conductivity and a high degree of oxygen disorder along the oxygen channels.

In recent computer simulation studies,^[20] we investigated the atomic-scale mechanisms of oxide-ion conduction in two apatite compounds, La₈Sr₂Si₆O₂₆ and La_{9.33}Si₆O₂₆. Our calculations predicted a complex, nonlinear interstitial mechanism along the O(5) channels with an activation energy consistent with experimental values. Crucial to this mechanism was the local cooperative distortion of the [SiO₄]⁴⁻ substructure. In addition, a previously unsuspected low-energy anion interstitial position was predicted to lie at the O(5) channel periphery, close to the [SiO₄]⁴⁻ tetrahedra. The existence of this interstitial position has since been confirmed by experiment, with the neutron diffraction studies of León-Reina et al.^[12] revealing that a similar site is partially occupied in La_{9.55}Si₆O_{26.32}, La_{9.6}Si₆O_{26.4}, and La_{9.6}Ge₆O_{26.4} systems. Mössbauer studies^[13] also indicate Fe³⁺ to be fivefold coordinated in La₁₀Si₅FeO_{26.5}, and recent ²⁹Si NMR studies^[16] have highlighted the importance of the silicate substructure to ionic conductivity. These results provide additional evidence for the validity of our potential model and the simulation approach used here.

Despite this success, our understanding of the atomic-level behavior of these apatite oxide-ion conductors is still incomplete. There is limited information on cation doping and defect processes at the local structural level, particularly the role of dopants on the Si site and the effect of vacancies in the La-occupied channels. There are also important questions relating to the dopant site selectivity and compensation mechanisms in these complex materials, the understanding of which is key to their optimization for use in solid oxide fuel cells or ceramic membranes.

Extended X-ray absorption fine structure (EXAFS) spectroscopy is ideally suited to the experimental investigation of such defect processes, because, unlike techniques such as X-ray or neutron diffraction, it does not measure long-range order but only the local environment of a particular atomic species.^[21] Used in conjunction with atomistic modeling techniques it can provide a powerful tool for investigating local structure and disorder. In this work, well-established atomistic modeling techniques^[22–25] are used for the first time to investigate the site selectivity and incorporation mechanisms of a range of M⁺, M²⁺, M³⁺, and M⁴⁺ dopants in an apatite of composition La_{9.33}Si₆O₂₆, constituting a wider survey of dopants than previous reports. We have also probed, using EXAFS and

simulation, the local structural distortion caused by key dopants and lattice defects.

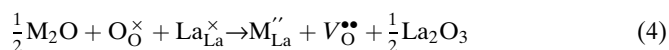
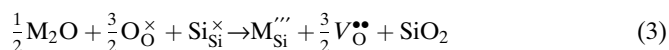
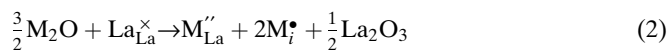
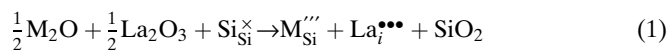
2. Results and Discussion

2.1. Defect Mechanisms of Dopant Incorporation

Experimental studies have shown that a broad range of dopants can be incorporated in lanthanum silicate apatite systems. The aliovalent doping of Ga³⁺ and Al³⁺ on the Si site is known to significantly enhance ionic conductivity,^[8,10] and the replacement of La³⁺ by larger alkaline-earth cations (e.g., Sr²⁺ and Ba²⁺) is also known to occur readily.^[12] Charge compensation in these systems is often achieved through the filling of vacant lanthanum sites, e.g., La_{9.33–2x/3}M_xSi₆O₂₆ (M = divalent cation) and La_{9.33+x/3}Si_{6–x}M_xO₂₆ (M = trivalent cation), although samples containing excess (interstitial) oxygen have also been synthesized.^[4,5,8,12] When transition metals are introduced, the picture is even more complex as the oxidation state of the dopant is often not known.

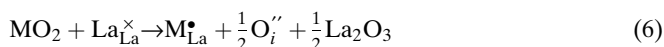
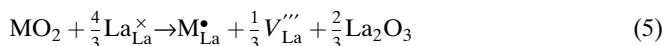
Our simulation methods can address key doping issues and provide quantitative estimates of the relative energies of different mechanisms of defect formation and dopant incorporation (referred to hereafter as “solution energies”), as has been done in related studies of ion-conducting oxides.^[26,27] We stress that although calculations are performed at infinite dilution, they can provide a useful guide to the likely site selectivity and compensation mechanisms of different dopants and to trends in dopant solubility.

We have examined the solution energies of a wide range of M⁺, M²⁺, M³⁺, and M⁴⁺ dopants on Si and La positions in La_{9.33}Si₆O₂₆. Two mechanisms of charge compensation for aliovalent dopants were investigated, which reflect experimentally employed doping strategies; i) the maintenance of constant oxygen content through the use of cation incorporation and deficiency, and ii) the use of oxygen vacancies and interstitials so as to maintain constant cation stoichiometry. For example, the substitution of monovalent (M⁺) dopants at constant oxygen stoichiometry and constant cation stoichiometry can be represented by the following defect equations (in Kröger–Vink notation) normalized to a single dopant substitutional, M



where M_{Si} indicates the dopant substitutional, V_O^{••} indicates an oxygen vacancy, and the interstitial defects (M_i[•] and La_i^{•••}) occupy the vacant La(1) sites. The same types of defect equa-

tions apply for divalent and trivalent dopants (which are given as Supporting Information S1). Of course, isovalent substitutions for La (by M^{3+}) and for Si^{4+} (by M^{4+}) do not require charge compensation. For M^{4+} doping on the La site, charge compensation can be accomplished by either using cation vacancies (for constant oxygen content) or by the inclusion of interstitial oxygen (for constant cation content), given by the following two equations



It is noted that although we have focused on these mechanisms, further work on oxygen excess mechanisms are being explored. As in previous studies,^[26,27] the energies of the dopant incorporation (or solution) reactions have been derived by combining the appropriate defect and lattice energy terms.

2.1.1. M^+ Dopants

First, our calculated energies of solution for monovalent dopants as a function of ion size are presented in Figure 2. We note that the radii for ions in sixfold coordination compiled by Shannon^[28] are used throughout, as values for four-, seven-, and nine-coordination are not available for all the ions considered here. In any case, our primary concern is to examine the difference in energies between substitution on the La and Si sites, which will not be affected by relative shifts in the ionic radii. Examination of our results reveals a clear preference for monovalent dopants (e.g., Na^+ and K^+) to substitute into the La(1) site, with compensation from incorporation of additional cations (Eq. 2). Substitution into the Si site (Eqs. 1 and 3) is predicted to be strongly unfavorable, irrespective of the compensation mechanism.

Only a few experimental studies have examined monovalent doping in the silicate-based apatite systems, largely because of

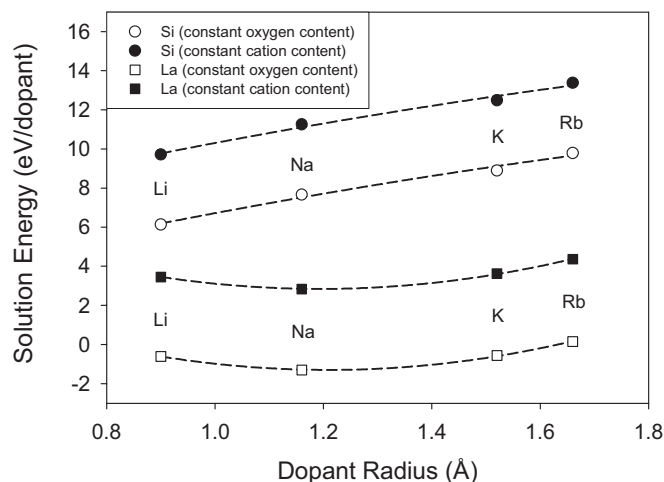


Figure 2. Calculated solution energies as a function of ionic radius for doping of M^+ into $La_{9.33}Si_6O_{26}$ in La(1) and Si sites.

problems with dopant oxide volatilization at the high synthesis temperatures used. Doping of Li and Na has been reported for the yttrium silicate systems $LiY_9Si_6O_{26}$ and $NaY_9Si_6O_{26}$,^[29] while for the wider apatite families, Li, Na, and K are known to substitute into the phosphate and sulfate analogues.^[30] In all cases, the doping occurs in cation channel positions (analogous to the La(1) positions in our system), which accords well with our results.

2.1.2. M^{2+} Dopants

Second, divalent dopants are common additives to apatite systems, particularly the alkaline earths, which can substitute for La in relatively large concentrations. We have again considered both mechanisms in our study, that is, doping at constant oxygen and cation stoichiometry. Our calculated solution energies for a series of divalent substitutions are presented in Figure 3 and again indicate a strong preference for dopants to

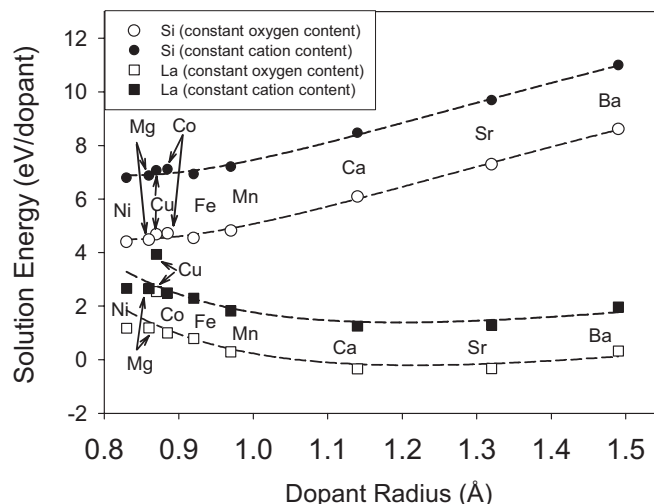


Figure 3. Calculated solution energies as a function of ionic radius for doping of M^{2+} into $La_{9.33}Si_6O_{26}$ in La(1) and Si sites.

substitute onto the La(1) site, in accord with observation. Compensation by means of interstitial cations is calculated to be the preferred mechanism for all dopants. We note, however, that the calculated solution energies for oxygen vacancy compensation on the La(1) site are also relatively low, especially for the larger alkaline earth dopants. This suggests that the generation of oxygen vacancies may be possible under appropriate experimental conditions.

The most notable feature of these results is the wide range of ion sizes (from 0.8 to 1.5 Å) over which divalent doping for La^{3+} is predicted to be favorable (relative to Si substitution). This can be taken as an indication of the flexibility of the structure, a point we return to below. These predictions also agree well with synthesis work, in which ions as different in size as Mg^{2+} (ionic radius, $IR=0.86$ Å) and Ba^{2+} ($IR=1.49$ Å) are observed to successfully substitute for La.^[8] This is a considerably broader range than that observed for doping into a single site

in most oxide-ion conductors, such as the LaGaO_3 perovskite, and highlights the breadth of doping regimes available for the apatite systems.

The lowest energy for incorporation of alkaline-earth dopants on the Si site is found for Mg^{2+} . This suggests possible “ambi-site” dopant behavior, with Mg^{2+} able to substitute simultaneously for both La and Si, recently confirmed by experiment.^[17] However, the solubility is predicted to be much greater on the La(1) site, so equal partitioning of the dopant between both La and Si sublattices is not expected. Our simulations also suggest that divalent transition metal ions (e.g., Ni^{2+}) are favorable dopant species and therefore warrant further investigation in the preparation of potential mixed ionic–electronic conductors (e.g., for use as separation membranes or SOFC electrodes). Following on from these modelling results, we have recently shown Ni substitution for La to be successful.^[17]

2.1.3. M^{3+} Dopants

Third, the replacement of La^{3+} with trivalent ions does not require charge compensation. For trivalent doping onto the Si site, both constant oxygen content and oxygen vacancy mechanisms were again considered. Our calculated solution energies for M^{3+} doping (Fig. 4) reveal more variation than those for M^+ and M^{2+} ions, with crossovers in minimum energy as the dopant size changes. With increasing dopant size, substitution onto the Si site becomes steadily less favorable, whilst the energy for solution onto the La(1) site decreases for larger dopants. The effect is such that for ions smaller than 0.7 Å (e.g., Al^{3+}) the Si site is preferred, although the results for Ga are less clear cut. For dopants larger than 0.9 Å (e.g., Y^{3+} and Nd^{3+}) the La(1) site is clearly favored.

In the range 0.70–0.85 Å, there exists a crossover region in which prediction of site preference is more difficult. Such a crossover region has been found from both EXAFS and modeling of other ion-conducting oxides, such as the CaZrO_3 and

BaCeO_3 perovskites,^[27] with possible “ambi-site” behavior in which ions can substitute for both host cations.

In addition, the oxidation state of the transition metal dopant ions in this region must be considered. In Table 1 we compare the results for M^{2+} and M^{3+} incorporation in both Si and La(1) sites for Co, Fe, and Mn. The most favorable dopants are M^{2+} species (Co^{2+} , Mn^{2+} , and Fe^{2+}) on the La(1) site, which sug-

Table 1. Solution energies for divalent and trivalent transition metal dopants in La(1) and Si sites.

Atom type	Solution energy (eV/dopant)			
	M^{2+} on Si site	M^{2+} on La(1) site	M^{3+} on Si site	M^{3+} on La(1) site
Mn	4.82	0.29	3.35	2.43
Fe	4.54	0.79	3.00	2.30
Co	4.72	1.00	2.83	3.00

gests higher solubility for these divalent dopants. For the M^{3+} species, there is a slight preference for Co^{3+} on Si, and for Mn^{3+} and Fe^{3+} on La(1), although there are uncertainties on account of the large lattice energies that are subtracted from each other to obtain the solution energies. These results are consistent with our experimental work on Co doping as well as results for the Mn-substituted phase;^[15] Co^{2+} and Mn^{2+} are seen to prefer the La(1) site, whilst Co^{3+} and Mn^{3+} substitute for Si. It is also observed that the solubility limit for Mn replacing Si is considerably lower than for La. Recent experimental results^[15] also suggest that these M^{3+} dopants are unstable on La sites with respect to M^{2+} , so that any M^{3+} species convert to M^{2+} .

2.1.4. M^{4+} Dopants

Finally, synthesis work on M^{4+} doping has so far concentrated on Ge^{4+} , which is found to form a continuous solid solution, $\text{La}_{9.33}\text{Si}_{6-x}\text{Ge}_x\text{O}_{26}$, where $0 < x < 1$.^[9] Our calculated solution energies (Fig. 5) predict that M^{4+} doping is strongly

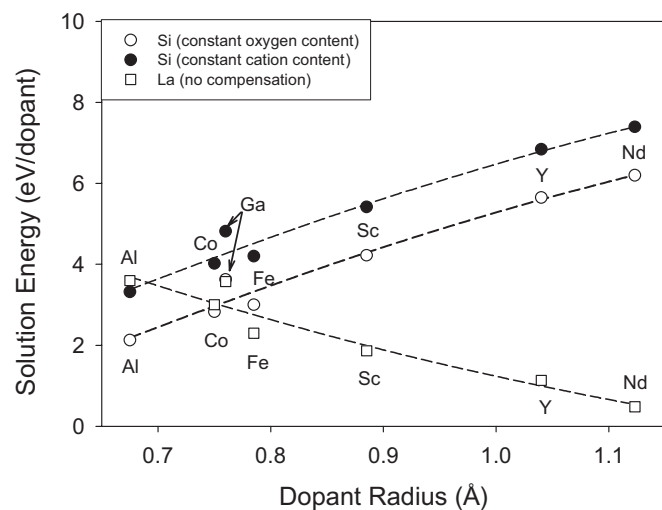


Figure 4. Calculated solution energies as a function of ionic radius for doping of M^{3+} into $\text{La}_{9.33}\text{Si}_6\text{O}_{26}$ in La(1) and Si sites.

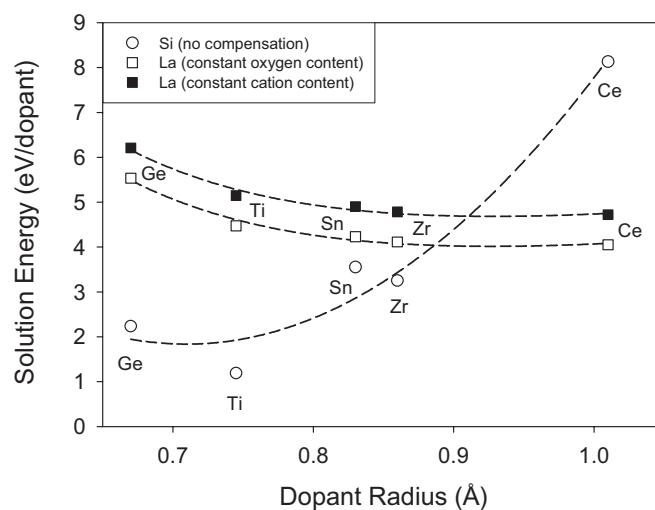


Figure 5. Calculated solution energies as a function of ionic radius for doping of M^{4+} into $\text{La}_{9.33}\text{Si}_6\text{O}_{26}$ in La(1) and Si sites.

unfavorable on the La(1) site and that Ge^{4+} is a favorable dopant for Si^{4+} . A strong correlation with dopant size is found for dopant substitution onto the Si site, such that Ce^{4+} is predicted to be unfavorable on both Si and La sites. Our results do, however, predict that doping of Ti^{4+} on the Si site is possible as found in zeolite materials. Indeed, recent experimental studies have confirmed this, with successful doping of up to 33 at % Ti on the Si site.^[9]

2.2. Local Structure around Dopants and Vacancy Defects

It has been found that fully stoichiometric systems, such as $\text{La}_8\text{Sr}_2\text{Si}_6\text{O}_{26}$, generally exhibit poor conductivity, whilst the doping of subvalent cations (such as Ga^{3+} or Al^{3+}) on the Si site,^[8,10] or La substoichiometry to create cation vacancies (on the La(1) positions),^[7] markedly improves conductivity. However, the effect of dopants on the local structure at the atomic level is still unclear. We have therefore investigated, using EXAFS and computer modeling, the local structural effects of the Ga^{3+} dopant on Si, and the Ba^{2+} dopant on La(1), as well as the La(1) vacancy in $\text{La}_{9.33}\text{Si}_6\text{O}_{26}$.

First, the structural parameters obtained from our analysis of the local structure around a Si ion, and a Ga dopant on a Si site, in $\text{La}_{9.66}\text{Si}_5\text{GaO}_{26}$ and $\text{La}_{10}\text{Si}_4\text{Ga}_2\text{O}_{26}$, are presented in Table 2, with the corresponding fitted data shown in Figures 6 and 7. For both the Si- and Ga-edge data, only the first shell M–O bond lengths were fitted, because of the complexity of the structure beyond the first shell.

Table 2. Final EXAFS models for $\text{La}_{9.66}\text{Si}_5\text{GaO}_{26}$ and $\text{La}_{10}\text{Si}_4\text{Ga}_2\text{O}_{26}$ indicating Si/Ga–O first shell separations

Composition	Edge	Coordination number	1st shell separation [Å]	R fit [%]
$\text{La}_{9.66}\text{Si}_5\text{GaO}_{26}$	Si–K	4	1.59	41.28
	Ga–K	4	1.82	39.10
$\text{La}_{10}\text{Si}_4\text{Ga}_2\text{O}_{26}$	Si–K	4	1.58	38.46
	Ga–K	4	1.82	38.35

Initial data analysis, including coordination number refinement, indicates a four-coordinate environment for both edges; the coordination number was thus fixed to this value for final refinements. First shell Si–O bond distances of ca. 1.58 Å were obtained for all samples; for the Ga edge, a value of 1.82 Å was obtained for Ga–O distances (Table 2). There is thus a marked difference in the local structure surrounding the Si and dopant species. This is in accord with the increase in site volume that would be expected from the relative ionic radii ($\text{IR} = 0.40$ Å for Si^{4+} , and 0.61 Å for Ga^{3+}). To complement this work, atomistic simulations of the local environments around an undoped Si site and a Ga-doped Si site were carried out; the interatomic separations are presented in Table 3. The local structure around an undoped Si site is illustrated in Figure 8.

In common with the EXAFS results, our atomistic simulations show a significant expansion of the tetrahedral unit upon

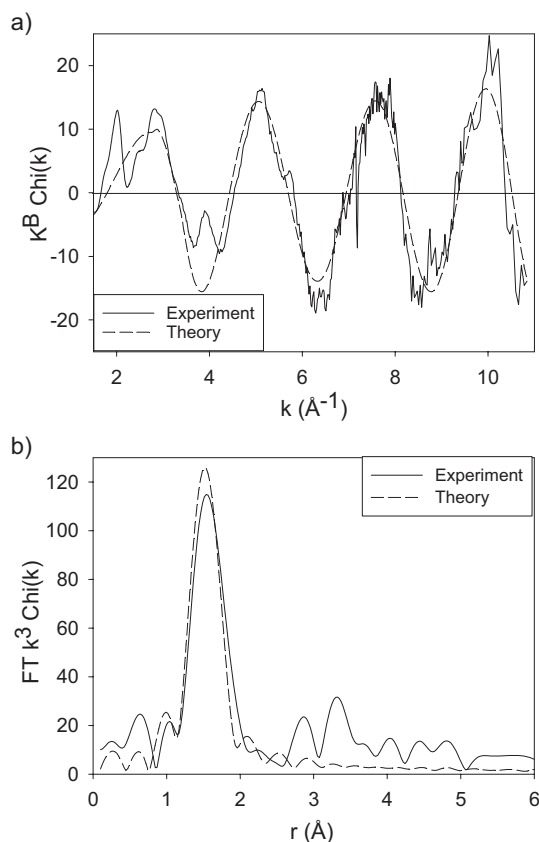


Figure 6. Fitted Si K-edge spectra for $\text{La}_{9.66}\text{Si}_5\text{GaO}_{26}$; a) EXAFS, b) Fourier transform.

Table 3. Calculated changes in local interatomic separations around a Ga^{3+} dopant in the Si site of $\text{La}_{9.33}\text{Si}_6\text{O}_{26}$

Ion pairs (M = Si or Ga)	Initial mean separation (M = Si) [Å]	Change in separation after Ga doping (M = Ga) [Å]
M–O(1,2,3,4)	1.63	+0.22
M–O(5)	3.83	0.00
M–La(1,2)	3.65	–0.05
La(1)–O(1,2)	2.53	–0.10
La(2)–O(1,2)	2.73	–0.18
O(1)–O(5)	4.28	–0.06
O(3)–O(5)	3.47	+0.05
O(4)–O(5)	3.56	–0.03

replacement of Si with Ga^{3+} , with the distances to oxygen increasing by 0.22 Å (Table 3). From our calculated distances it can be seen that there are other structural changes and, in particular, the accommodation of this expansion by the rest of the crystal is significant. Relatively small changes are predicted for the O(1)–O(5), O(3)–O(5), and O(4)–O(5) distances, with the calculated M–O(5) separation remaining unchanged upon Ga incorporation. In contrast, a significant contraction in the La(1)–O(1,2) and La(2)–O(1,2) distances is found. In general these results suggest that the local distortions accompanying Ga dopant incorporation on the Si site are accommodated by

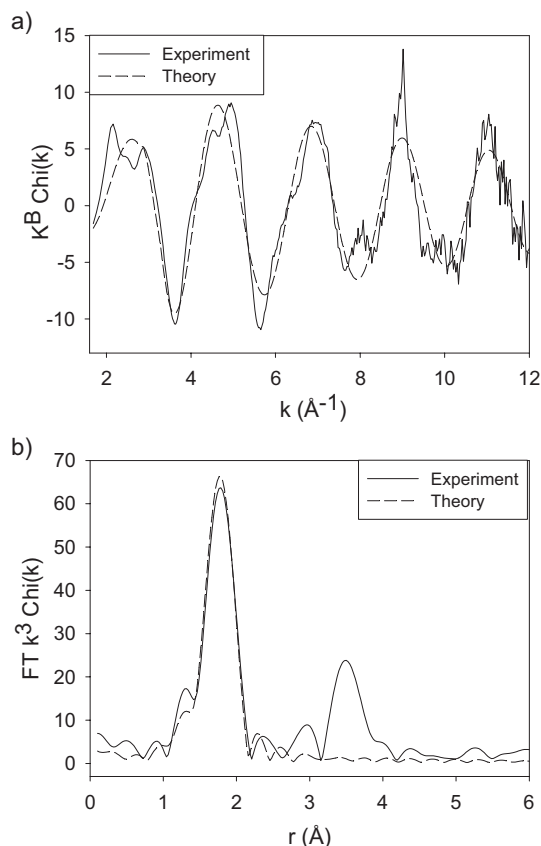


Figure 7. Fitted Ga K-edge spectra for $\text{La}_{9.66}\text{Si}_5\text{GaO}_{26}$: a) EXAFS, b) Fourier transform.

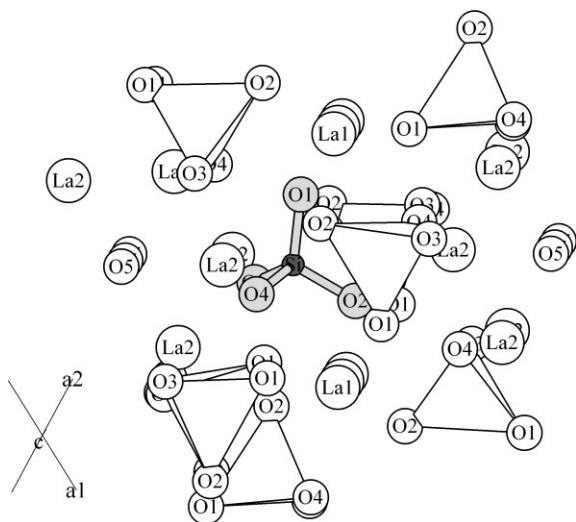


Figure 8. Local structure in $\text{La}_{9.33}\text{Si}_6\text{O}_{26}$ with atom labels and an SiO_4 unit highlighted.

the La(1) channels rather than the O(5) conduction channels. Thus, the oxygen channels are kept open for ion conduction, in agreement with the high conductivities observed for such Ga-doped samples.

Second, our calculated interatomic separations from simulations of the local structural effects of a La vacancy, or a Ba^{2+} dopant on a La(1) site in $\text{La}_{9.33}\text{Si}_6\text{O}_{26}$ are presented in Table 4.

Strong distortion of the lattice is predicted to occur around both the La vacancy and the Ba dopant. Interestingly, the introduction of Ba on the La(1) site has a very similar, although less pronounced, effect to a La vacancy. Most prominent is the

Table 4. Calculated changes in local interatomic separations around an intrinsic La vacancy and a Ba^{2+} dopant in the La(1) site of $\text{La}_{9.33}\text{Si}_6\text{O}_{26}$.

Ion pair [a]	Initial mean separation with M = La [Å]	Change in separation after removing La [Å]	Change in separation with M = Ba [Å]
M–O(1)	2.41	+0.40	+0.25
M–O(2)	2.54	+0.15	+0.14
M–O(3)	2.82	+0.43	+0.21
M–O(4)	4.94	+0.34	+0.28
M–Si	3.31	+0.08	+0.11
M–Si	3.64	+0.14	+0.12
M–La(1)	3.63	–0.32	–0.09
O(1)–O(5)	4.24	–0.15	–0.11
O(3)–O(5)	3.34	–0.13	–0.14
O(4)–O(5)	3.07	+0.39	+0.39

[a] M = Ba, La, or vacancy.

displacement of the nearest-neighbor oxygen positions and the effect on the $[\text{SiO}_4]^{4-}$ substructure. Distances to O(1) and O(3) sites are calculated to lengthen by up to 15% when La is replaced by Ba or when the site is vacant. The local changes give rise to a tilting of the $[\text{SiO}_4]^{4-}$ units immediately adjacent to the Ba dopant or La vacancy. The effect of this change on the O(5) oxide channel is shown by the shortening of the O(1)–O(5) and O(3)–O(5) distances, and the significant lengthening of the O(4)–O(5) separation. The overall effect is thus to cause an outward displacement of nearby $[\text{SiO}_4]^{4-}$ units, so that more of the O(1)–O(3)–O(4) face is shown to the O(5) channel, which could be important for ion conduction. This is in marked contrast to our earlier EXAFS results for the smaller Co^{2+} dopant in this site, which revealed a general contraction of the surrounding structure.^[15]

Some discussion of the coordination environment surrounding this site is also relevant at this point. Normally, the La(1) position is regarded as having a distorted environment, with six close anion neighbors and three slightly more distant. From structural work on $\text{La}_{9.33}\text{Si}_6\text{O}_{26}$, these two “shells” have been found to lie at ca. 2.5 Å and 2.9 Å, representing a difference in separation of ca. 14%. In our simulations, this separation remains constant when La is partially replaced with Ba, and increases slightly around a La vacancy. However, our previous results from EXAFS of the smaller Co^{2+} dopant in this site show a much larger separation (>20%) for the six- and three-coordinate shells.^[15] This suggests that the unusually broad range of dopants that can be incorporated onto this La position results from the flexibility of the surrounding silicate substructure.

ture, which allows large local changes in site volume and coordination.

3. Conclusions and Outlook

Apatite-type silicates have been attracting considerable interest as a new family of oxide-ion conductors with potential use in solid oxide fuel cells and oxygen-permeable membranes. Our combined computer simulation and EXAFS studies have provided new insights into the dopant behavior of these functional materials, based on quantitative results at the atomic-level as opposed to qualitative arguments.

The results first indicate that an unusually broad range of dopant ions (in size and charge state) can substitute for La in the $\text{La}_{0.33}\text{Si}_6\text{O}_{26}$ apatite, in accord with the available synthesis studies. The range of dopants is much wider than that observed for doping on a single cation site in most other ionic conductors for fuel cell applications, such as perovskite-type oxides. In addition, our local structural investigation demonstrates that this dopant behavior is related to the flexibility of the silicate substructure, which allows relatively large local distortion and alteration of the site volumes. In our view, this is a key factor in the high oxide-ion conductivity exhibited by these apatite silicates, warranting further investigation. Indeed, the breadth of possible doping regimes in these novel materials provides new opportunities to design and optimize the conduction properties for fuel cell electrolytes.

4. Experimental

Materials Synthesis and Characterization: Ga-doped samples were prepared by way of solid-state reaction of La_2O_3 , SiO_2 , and Ga_2O_3 . The dried starting materials were ground together in the appropriate ratios and heated twice at high temperature. Compositions $\text{La}_{0.66}\text{Si}_5\text{GaO}_{26}$ and $\text{La}_{10}\text{Si}_4\text{Ga}_2\text{O}_{26}$ were initially calcined for 12 h at 1300°C , then again at 1350°C . Between firings the samples were reground to ensure homogeneous reaction. Phase purity was confirmed using a Seifert 3003TT laboratory powder X-ray diffractometer, and full structure characterization achieved using neutron powder diffraction, the results of which have been reported elsewhere [8]. EXAFS measurements were performed using the 2 GeV Synchrotron Radiation Source (SRS) at Daresbury Laboratory, UK. Data were collected using two instruments, one for the Si–K edge (at 1.84 keV), and the other for the Ga–K edge (at 10.37 keV). Twin single crystal monochromators (InSb(111) for the former, and Si(111) for the latter) were used for wavelength selection. Because of absorption effects, all data were collected in fluorescence mode, with several scans performed for each sample, and the data thus obtained summed to reduce statistical noise. Data analysis was performed using the Daresbury suite of EXAFS software EXCALIB, EXSPLINE, and EXCURV98. The fitting was performed in k -space and the data was k^3 -weighted for refinement. For both the Si and Ga edge data, only the first shell M–O bond lengths were fitted because of the complexity of the structure beyond the first shell. Indeed, because of the poor resolution of the second shell in all data, no structurally sensible information could be obtained for shells other than the first, and so it was chosen to leave further shells unfitted. For doping of the Si site, EXAFS data for both dopant and Si edges are presented, although the quality of the Si-edge data was found to be inferior to that of the Ga-edge because of difficulties with sample alignment. This resulted in difficulties in fitting and slightly anomalous Debye–Waller values were obtained for the Si-edge data. It should be noted that this

affected the Debye–Waller factors much more than the radial distances.

Computer Modeling: The computational study used well-established atomistic modeling techniques, as embodied in the GULP code [22]. These methodologies are extensively documented elsewhere [23], so only a brief summary is given here. Interactions between ions are evaluated as the sum of long-range Coulombic terms and short-range interactions modeled by the Buckingham interatomic potential (which takes account of Pauli repulsion and van der Waals effects). The shell model was used to provide a simple yet effective description of polarizability effects. A well established three-body term for the angle-dependent SiO_4 tetrahedral unit was also used, which has proved successful in the modeling of a wide range of silicates, zeolites and hydroxyapatites [24,25]. For this investigation we have chosen to study the $\text{La}_{0.33}\text{Si}_6\text{O}_{26}$ composition, as it provides a good reference stoichiometry for a wide variety of doping regimes. Interatomic potentials were transferred directly from our previous study [20], which accurately reproduce the observed complex structure of space group $P\bar{3}$ (Table 5). For this work, calculations were based upon a $1 \times 1 \times 3$ supercell (124 atoms, $P1$ symmetry) of the $\text{La}_{0.33}\text{Si}_6\text{O}_{26}$ crystallographic unit cell [7], with periodic boundary conditions applied to simulate a bulk crystal. In accordance

Table 5. Calculated and experimental structural parameters for $\text{La}_{0.33}\text{Si}_6\text{O}_{26}$.

Parameter	Experimental [7] [Å]	Calculated [Å]
a/b	9.7248	9.7607
c	7.1895	7.1198
Si–O	1.6231	1.6271
La(1)–O	2.6437	2.6493
La(2)–O	2.4931	2.4965

with previous experimental and simulation work, which shows dopants and defects to favor the La(1) channel positions, the two La vacancies in the supercell of $\text{La}_{0.33}\text{Si}_6\text{O}_{26}$ were placed in La(1) sites. The lowest energy configuration was found to have, as expected, the largest interatomic separation between vacancies, which was used as the structural model for all the calculations. The interatomic potentials and lattice energies used for our dopant calculations are available as Supporting Information (S2).

An important feature of our simulations is the treatment of lattice relaxation around the point defect or dopant ion. In this work, the Mott–Littleton approach [22,23] was employed, in which the crystal lattice is partitioned into two regions; the immediate environment surrounding the defect is relaxed explicitly (ca. 750 ions), whilst the remainder of the crystal (>8000 ions), where the defect forces are relatively weak, is treated by more approximate quasi-continuum methods. In this way, the full relaxation around the defect can be modeled effectively, since the crystal is not considered simply as a rigid lattice.

Received: August 29, 2006

Revised: October 30, 2006

Published online: August 21, 2007

- a) B. C. H. Steele, A. Heinzl, *Nature* **2001**, *414*, 345. b) A. Atkinson, S. Barnett, R. J. Gorte, J. T. S. Irvine, A. J. Mcevoy, M. Mogensen, S. C. Singhal, *Nat. Mater.* **2004**, *3*, 17.
- a) R. M. Ormerod, *Chem. Soc. Rev.* **2003**, *32*, 17. b) Z. P. Zhou, S. M. Haile, *Nature* **2004**, *431*, 170.
- a) M. Mamak, G. S. Metraux, S. Petrov, N. Coombs, G. A. Ozin, M. A. Green, *J. Am. Chem. Soc.* **2003**, *125*, 5161. b) S. Tao, J. T. S. Irvine, J. A. Kilner, *Adv. Mater.* **2005**, *17*, 1734.

- [4] a) S. Nakayama, T. Kagayama, H. Aono, Y. Sadoaka, *J. Mater. Chem.* **1995**, *5*, 1801. b) H. Arikawa, N. Nishiguchi, T. Ishihara, Y. Takita, *Solid State Ionics* **2000**, *136–137*, 31. c) S. Nakayama, Y. Higuchi, Y. Kondo, M. Sakamoto, *Solid State Ionics* **2004**, *170*, 219.
- [5] S. Tao, J. T. S. Irvine, *Mater Res. Bull.* **2001**, *36*, 1245.
- [6] a) H. Yoshioka, S. Tanase, *Solid State Ionics* **2005**, *176*, 2395. b) Y. Masubuchi, M. Higuchi, T. Takeda, S. Kikkawa, *Solid State Ionics* **2006**, *177*, 263.
- [7] J. E. H. Sansom, D. Richings, P. R. Slater, *Solid State Ionics* **2001**, *139*, 205.
- [8] a) J. E. H. Sansom, J. R. Tolchard, P. R. Slater, M. S. Islam, *Solid State Ionics* **2004**, *167*, 17. b) A. Najib, J. E. H. Sansom, J. R. Tolchard, P. R. Slater, M. S. Islam, *Dalton Trans.* **2004**, 3106.
- [9] a) J. E. H. Sansom, A. Najib, P. R. Slater, *Solid State Ionics* **2004**, *175*, 353. b) J. E. H. Sansom, P. A. Sermon, P. R. Slater, *Solid State Ionics* **2005**, *176*, 1765.
- [10] E. J. Abram, D. C. Sinclair, A. R. West, *J. Mater. Chem.* **2001**, *11*, 1978.
- [11] a) L. León-Reina, M. C. Martín-Sedeno, E. R. Losilla, A. Cabeza, M. Martínez-Lara, S. Bruque, F. M. B. Marques, D. V. Sheptyakov, M. A. G. Aranda, *Chem. Mater.* **2003**, *15*, 2099. b) L. León-Reina, E. R. Losilla, M. Martínez-Lara, S. Bruque, A. Llobet, D. V. Sheptyakov, M. A. G. Aranda, *J. Mater. Chem.* **2005**, *15*, 2489.
- [12] L. León-Reina, E. R. Losilla, M. Martínez-Lara, S. Bruque, M. A. G. Aranda, *J. Mater. Chem.* **2004**, *14*, 1142.
- [13] V. V. Kharton, A. L. Shaula, M. V. Patrakeev, J. C. Waerenborgh, D. P. Rojas, N. P. Vyshatko, E. V. Tsipis, A. A. Yaremchenko, F. M. B. Marques, *J. Electrochem. Soc.* **2004**, *151*, A1236.
- [14] a) V. Maisonnueve, E. Leduc, O. Bohnke, M. Leblanc, *Chem. Mater.* **2004**, *16*, 5220. b) E. Rodriguez-Reyna, A. F. Fuentes, M. Maczka, J. Hanuza, K. Boulahya, U. Amador, *J. Solid State Chem.* **2006**, *179*, 522.
- [15] J. R. Tolchard, J. E. H. Sansom, M. S. Islam, P. R. Slater, *Dalton Trans.* **2005**, 1273.
- [16] J. E. H. Sansom, J. R. Tolchard, M. S. Islam, D. Apperley, P. R. Slater, *J. Mater. Chem.* **2006**, *16*, 1410.
- [17] E. Kendrick, J. R. Tolchard, J. E. H. Sansom, M. S. Islam, P. R. Slater, *Faraday Discuss.* **2007**, *134*, 181.
- [18] S. Celerier, C. Laberty-Robert, J. W. Long, K. A. Pettigrew, R. M. Stroud, D. R. Rolison, F. Ansart, P. Stevens, *Adv. Mater.* **2006**, *18*, 615.
- [19] a) Q. H. Shi, J. F. Wang, J. P. Zhang, J. Fan, G. D. Stucky, *Adv. Mater.* **2006**, *18*, 1038. b) J. H. Zhan, Y. H. Tseng, J. C. C. Chan, C. Y. Mou, *Adv. Funct. Mater.* **2005**, *15*, 2005. c) G. He, T. Dahl, A. Veis, A. George, *Nat. Mater.* **2003**, *2*, 552.
- [20] a) M. S. Islam, J. R. Tolchard, P. R. Slater, *Chem. Commun.* **2003**, 1486. b) J. R. Tolchard, M. S. Islam, P. R. Slater, *J. Mater. Chem.* **2003**, *13*, 1956.
- [21] A. V. Chadwick, *Solid State Ionics* **1993**, *63–65*, 721.
- [22] J. D. Gale, *J. Chem. Soc. Faraday Trans.* **1997**, 629
- [23] C. R. A. Catlow, *Computer Modelling in Inorganic Crystallography*, Academic, San Diego **1997**.
- [24] a) M. Colligan, P. M. Forster, A. K. Cheetham, Y. Lee, T. Vogt, J. A. Hriljac, *J. Am. Chem. Soc.* **2004**, *126*, 12015. b) A. A. Sokol, C. R. A. Catlow, J. M. Garces, A. Kuperman, *Adv. Mater.* **2000**, *12*, 1801.
- [25] a) N. H. de Leeuw, D. Mkhonto, *Chem. Mater.* **2003**, *15*, 1567. b) N. H. de Leeuw, *J. Phys. Chem. B* **2004**, *108*, 1809.
- [26] a) M. S. Islam, R. A. Davies, *J. Mater. Chem.* **2004**, *14*, 86. b) M. S. Islam, D. Driscoll, C. A. J. Fisher, P. R. Slater, *Chem. Mater.* **2005**, *17*, 5085.
- [27] a) J. Wu, R. A. Davies, M. S. Islam, S. M. Haile, *Chem. Mater.* **2005**, *17*, 846. b) R. A. Davies, M. S. Islam, A. V. Chadwick, G. E. Rush, *Solid State Ionics* **2000**, *130*, 115.
- [28] R. D. Shannon, *Acta Crystallogr. A* **1976**, *32*, 751.
- [29] G. R. Redhammer, G. Roth, *Acta Crystallogr. Sect. C* **2003**, *59*, I120.
- [30] A. Laghzizil, P. Barboux, A. Bouhaouss, *Solid State Ionics* **2000**, *128*, 177.